Nuclear Materials and Energy 48 (2026) 102210

Contents lists available at ScienceDirect

Nuclear Materials and Energy

journal homepage: www.elsevier.com/locate/nme

Wire electron beam additive manufacturing for monoblock HCPB breeding blanket components: Preliminary assessment through experimental investigation☆

Gaurav Verma [a,*], Luděk Stratil [b], Jörg Rey [a], Bernd Baufeld [c], Martin Petersen [c], Stephen Fischer [a], Heiko Neuberger [a], Francisco A. Hernández [a], Jarir Aktaa [a]

[a] Karlsruhe Institute of Technology (KIT), 76344 Eggenstein-Leopoldshafen, Germany
[b] Institute of Physics of Materials, Czech Academy of Sciences, 61600 Brno, Czech Republic
[c] Pro-beam Additive GmbH, 82205 Gilching, Germany

ARTICLE INFO

Keywords:
Helium cooled pebble bed
DEMO
Wire electron beam additive manufacturing
Monoblock
HIP

ABSTRACT

The Helium-Cooled Pebble Bed (HCPB) Breeding Blanket (BB) is a key driver blanket concept for the EU DEMO fusion power plant, critical to achieving performance and long-term sustainability. However, its current design and fabrication present significant challenges. Conventional fabrication methods provide limited flexibility to meet these requirements. Additive Manufacturing (AM) has emerged as a promising alternative, already well established in the automotive and aerospace industries, but its application in the nuclear industry remains limited. For EU DEMO, several AM approaches have already been investigated for BB subcomponents. However, Wire Electron Beam Additive Manufacturing (WEBAM) remains underexplored despite its potential advantages. The present work provides a preliminary assessment of WEBAM's suitability for producing Monoblock HCPB BB components, supported by experimental trials for deposition scale effects and post-processing. Grade 92 ferritic-martensitic steel (X10CrWMoVNb9-2, P92) was selected for the experimental trials as a substitute for Eurofer97. In the experimental investigation, WEBAM samples of two different sizes were deposited on P92 substrates to examine the effects of increasing deposition volume on the microstructure, defect characteristics, and mechanical properties, as well as to assess the effectiveness of post-AM heat and hot isostatic pressing (HIP) treatment in mitigating the observed defects. Metallographic analyses, hardness measurements, and mechanical testing, including tensile and Charpy impact tests were performed to assess the properties of the AM material relative to those of the base material. Further, challenges associated with scaling and transferability of process and post-processing parameters from Gr.92 Steel to Eurofer97 are discussed in the present work.

1. Introduction

In the present EU DEMO design, the Helium-Cooled Pebble Bed (HCPB) Breeding Blanket (BB) is one of the primary driver blanket concepts and is essential for achieving both fusion power plant (FPP) performance and long-term sustainability [1,2]. As a multi-functional component, HCPB BB is expected to perform several mission critical functions. However, its current design and fabrication present major challenges, stemming from the highly complex geometry, large structural dimensions, numerous high-precision manufacturing steps, limited assembly space, the need for highly reliable joints, and stringent quality assurance requirements. These challenges prompted a new design solution which involves manufacturing the BB as a modular Monoblock component [3]. A Monoblock BB (Figure.1) refers to an architecture in which the First Wall (FW) and Breeder Zone (BZ) are constructed out of a single solid block. This innovative design, currently under development at KIT, is proposed as a promising solution to overcome the limitations associated with the existing BB reference design and its manufacturing routes.

Traditionally, manufacturing has relied heavily on processes such as casting, forging, and machining which are well suited for producing components from uniform materials but offer limited flexibility in

☆ This article is part of a special issue entitled: 'ICFRM-22' published in Nuclear Materials and Energy.

* Corresponding author.
E-mail address: gaurav.verma@kit.edu (G. Verma).

https://doi.org/10.1016/j.nme.2026.102210
Received 4 December 2025; Received in revised form 20 August 2026; Accepted 22 August 2026
Available online 24 August 2026

design. When it comes to creating customized, intricate geometries with advanced material requirements, these conventional approaches face significant limitations. In recent years, Additive Manufacturing (AM) has emerged as a promising alternative, enabling the fabrication of components with complex geometries. AM technologies are increasingly being adopted in industries such as automotive and aerospace, and have achieved a degree of standardization through different standards (ISO, SAE, ASTM, SAC), covering areas such as terminology, machines, process categories, feedstock, test methods, and guidelines [3–5].

In contrast, the nuclear industry – particularly in fission has seen only limited application of AM-fabricated components in reactors. One of the earliest notable examples comes from Oak Ridge National Laboratory, which, in collaboration with Framatome and the Tennessee Valley Authority (TVA), 3D printed fuel assembly channel fasteners and successfully installed them in TVA's Brown's Ferry nuclear power plant for irradiation studies [3,6–8]. Further, standardization for such developments in nuclear construction code (RCC-M [9]) is nearly absent. Nevertheless, this is an active area of research and development and several efforts are being made to address these gaps. ASME BPVC Section III [10] and Section IX [11] in recent versions have started publishing rules for additive techniques through approved code cases like Powder Metallurgy (PM) – Hot Isostatic Pressing (HIP) through ASME Code Case N-834, Gas Metal Arc Additive Manufacturing (GMAAM) through ASME Code Case 3020, etc. RCC-MRx also in its latest 2025 edition has incorporated qualification process for components produced using Laser-Powder Bed Fusion (LPBF) in its Probationary Phase Rules (RPP) under RPP27 [12].

In recent years, growth of Small Modular Reactors and the rapid push towards commercialization of fusion reactors have renewed interest in non-conventional manufacturing technologies, particularly AM. Taking advantage of this development, researchers have explored various AM techniques for fabricating FPP components. For EU DEMO BB and their subcomponents (such as the FW and internal structures), researchers have investigated numerous processes including LPBF like Selective Laser Melting (SLM) and Directed Energy Deposition (DED) methods like Cold Spray [3,13–16]. Each of these techniques presents specific advantages and limitations when applied to BB manufacturing.

Contrary to them, the technology of Wire Electron Beam Additive Manufacturing (WEBAM) remains underexplored despite its potential. WEBAM offers distinct benefits, including high deposition rates (adjustable through wire diameter), efficient material utilization, and the capability to produce complex geometries [17,18]. For example, WEBAM achieves deposition rates in the range of several kg/h, significantly higher than SLM. Also, in WEBAM, wire feed can reach very high material utilization, while SLM loses a fraction of powder through handling, sieving, and limited recyclability. Compared to Cold Spray, WEBAM can build free-standing, near-net parts. One of the main advantages unique to WEBAM when compared to both SLM and Cold Spray is its ability to pre-heat the substrate using electron beam (EB). WEBAM has already been widely applied in aerospace and defense industries with Titanium alloys for fabrication, repair and restoration [19,20] and in energy industry with Nickel and Steel based alloys [21,22]. Nevertheless, its application to fusion BB component manufacturing warrants further investigation.

Considering the future prospects of WEBAM, the primary objective is preliminary assessment of the suitability of the WEBAM process for manufacturing KIT Monoblock components. In the present study, this exploration is initiated by investigating scaling effects associated with increased deposition volume, the resulting scale-dependent defect evolution, and the role of post-processing, specifically post WEBAM heat treatment (HT) and hot isostatic pressing (HIP), in mitigating manufacturing defects. This is based on the underlying rationale that as the deposited volume increases during WEBAM, the thermal history and cooling rate are expected to change, potentially influencing the resulting microstructure, phase balance, and defect size and distribution.

Accordingly, the present work addresses four specific objectives. First, to investigate the influence of increasing deposition volume on the microstructure, defect characteristics, and mechanical properties of WEBAM-fabricated P92 steel. Second, to evaluate the effectiveness of post-WEBAM HT and HIP in modifying the microstructure and reducing manufacturing defects. Third, to compare the microstructural and mechanical properties of the additively manufactured Grade 92 material with those of conventional P92 steel material. Finally, to provide a preliminary assessment of the suitability of WEBAM for manufacturing monoblock-sized components, highlighting the challenges associated with process scaling and the transferability of process and post-processing parameters from Grade 92 steel to Eurofer97.

2. Material for fabrication

Although, Eurofer97 is the reference structural material candidate for EU DEMO BB which is a Reduced Activation Ferritic/Martensitic (RAFM) steel, its limited availability and relatively higher cost restrict its use in large-scale fabrication trials. Consequently, Grade 92 steel, also known as 9Cr-2W ferritic–martensitic (X10CrWMoVNb9-2) steel was selected for the fabrication trials as a practical alternative. The primary difference between Gr.92 steel and Eurofer97 lies in the stricter compositional control of certain alloying elements in Eurofer97 like Mo, Nb and Ni, along with the addition of Ta as Carbide/Nitride former. Nevertheless, the two steels exhibit very similar chemical compositions overall, resulting in comparable metallurgical behavior and therefore similar responses to manufacturing processes and HTs. Both materials develop closely related precipitate populations, dominated by $M_{23}C_6$ carbides and MX carbonitrides, while Grade 92 additionally forms Laves phase (M_2X) precipitates. A detailed comparison of the compositions of Eurofer97 [12] and Grade 92 [23] is provided in Table 1. Moreover, the

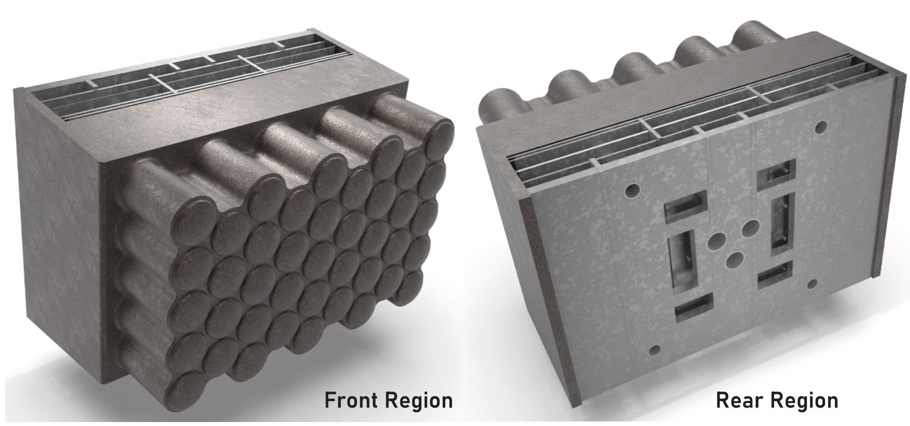

Fig. 1. A section of KIT Monoblock BB [3].

Table 1
Composition of Eurofer97 and Grade 92 Steel [12,23].

Elements	Eurofer97 (wt.%)	Gr. 92/P92 (wt.%)
C	0.09–0.12	0.07 – 0.13
Cr	8.5 – 9.5	8.5 – 9.5
W	1.0 – 1.2	1.5 – 2.0
Mo	ALAP, max 0.005	0.3 – 0.6
Mn	0.2 – 0.6	0.3 – 0.6
V	0.15 – 0.25	0.15 – 0.25
Ta	0.10 – 0.14	–
Nb	ALAP, max 0.005	0.04 – 0.09
N	0.015 – 0.045	0.03–0.07
B	max 0.002	0.001 – 0.006
Ni	max 0.01	max 0.4
Si	max 0.05	max 0.5
P	max 0.005	max 0.02
S	max 0.005	max 0.01

Note: ALAP – As Low as Possible.

use of commercial 9Cr steels (Grade 91/92) for DEMO BB manufacturing development is common practice in the European fusion community, owing to their ready availability and weldability behavior comparable to that of Eurofer97 [16,24].

3. Methodology

3.1. Fabrication of WEBAM components

To investigate the suitability of WEBAM for manufacturing HCPB BB components, two preliminary samples (denoted as PS1 and PS2) were first produced followed by a distributor cylinder. All specimens were manufactured on P92 steel substrates at the facilities of pro-beam additive GmbH, a company with extensive experience in WEBAM [25], as shown in Figs. 2–4. The WEBAM parameters were optimized for samples produced using ø1.0 mm wire (each in 15 kg spool coils) of material Thermanit MTS 616 with base material 1.4901 – X10CrWMoVNb9-2 (Grade 92). The elemental composition of Thermanit wire is tabulated in Table 2. This wire material is found to be suitable for welding P92 steels as per ASTM A 355 and these were supplied by Voestalpine Böhler [26].

The WEBAM jobs were performed on a pro-beam K40 machine in which the externally mounted vertical EB generator is operated at a voltage of 60 kV. Based on the parameter set developed for preliminary samples, a melt bead with Ø9 mm was obtained for the distributor cylinders. A linear trace of build material in three rows was done for the

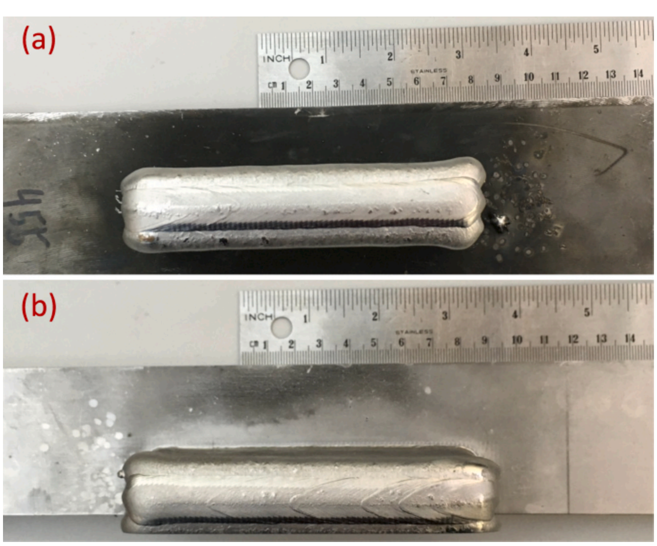

Fig. 2. WEBAM preliminary samples (a) PS1; (b) PS2.

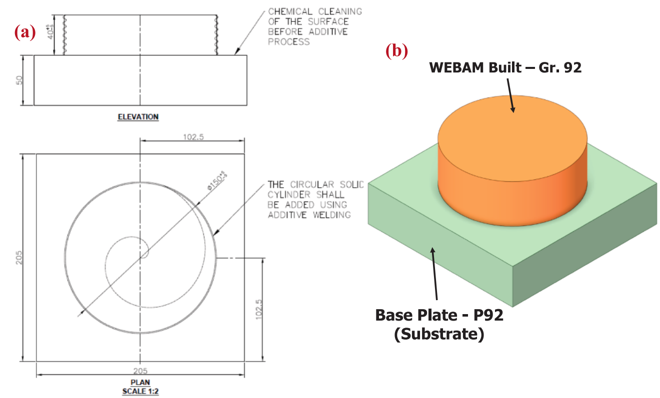

Fig. 3. WEBAM distributor cylinder (a) detailed drawing; (b) representative CAD model.

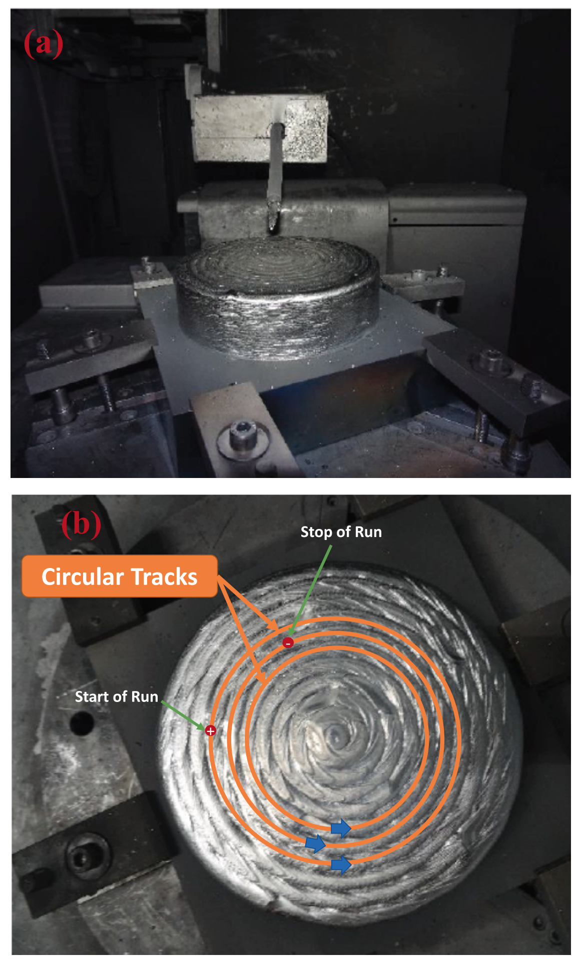

Fig. 4. WEBAM distributor cylinder (a) during manufacturing; (b) cylinder with 11 circular runs per layer.

Table 2
Composition of Thermanit MTS 616.[26].

Element	wt. %	Element	wt. %
C	0.11	Ni	0.7
Si	0.2	V	0.2
Mn	0.6	W	1.6
Cr	8.8	Nb	0.05
Mo	0.5	N	0.05

preliminary samples.

The distributor cylinder (ø150mm) was fabricated using a layer-wise deposition strategy using a circular trace. A total of 25 layers were deposited in the vertical direction. Each layer consisted of 11 circular runs of increasing diameter (Fig. 4a). A track is defined as a single continuous deposited bead produced during one uninterrupted torch movement (one run). To minimize heat accumulation and localized defects associated with start–stop locations, the start and stop positions of successive tracks were rotated by 72° (shown in Fig. 4b).

The WEBAM parameters for the production of distributor cylinder are presented in Table 3. The dimensions of preliminary samples of built materials were t x L x H: 30 mm x 140 mm x 56 mm and 30 mm x 150 mm x 57 mm for PS1 and PS2, respectively whereas dimensions for distributor cylinder built was D x H as 155.5 mm x 43 mm.

One of the advantages of EB technology is its unique capability to pre-heat the base plate already installed in high vacuum just before the WEBAM process. In order to measure the temperature during pre-heating, thermocouples were attached to the bottom (T1) and the top (T3) of the plate (as shown in Fig. 5a). During the pre-heating, the top of the plate was scanned over an area of 150 mm x 150 mm by EB with 4.2 kW for 27 min. The pre-heating was carried out for the surface temperature reaching above 650 °C as shown in Fig. 5b which is significantly higher than the reported thermocouple temperatures (Fig. 5c) as they were placed at a distance from the pre-heating area. Dye penetrant test of this additively manufactured cylinder was also carried out in order to obtain the surface defects (Fig. 6). No indications for cracks between the base plate and WEBAM built were found, however, some indications were observed on the top surface at the track stops but were not deep.

3.2. Heat and HIP treatment

Selected printed components and the sample blocks extracted from them by wire-EDM were subjected to heat treatment. Several HT conditions were designed to: (i) transform the as-printed (AP) microstructure of the components into a tempered martensitic microstructure, which is desirable for Grade 92 steel products, and (ii) homogenize the AP microstructure and suppress chemical heterogeneity that developed during layer-by-layer solidification and its consequent heating caused by thermal loading on successive layers depositions. In addition, HIP was applied to mitigate discontinuity-type defects, such as voids and hot cracks. A description of the extracted blocks and the applied HTs is provided in Table 4.

The preliminary sample PS1 was characterized in AP state. The preliminary sample PS2 was heat-treated after printing by tempering (750 °C/60 min). Subsequently, a selected block extracted from this sample by wire–EDM (shown in Fig. 7) was subjected to additional HT consisting of solution annealing in vacuum by 1150 °C/4h followed by quenching (1050 °C/30 min) and tempering (750 °C/90 min). PS1 was not heat treated and was tested in AP state.

From the distributor cylinder, five block samples were extracted

Table 3
WEBAM process parameters for distributor cylinder.

Parameter	Values
Beam Power (kW)	4.1–3.7
Beam Current (mA)	68–62
Lens Current (A)	1.7
Table Feed Speed (mm/s)	8.0
Wire Diameter (mm)	1.0
Wire Feed Rate (m/min)	7.5
Deposition Rate (kg/h)	3.41
Layer Height (mm)	1.7
Layer Number	25
Time between Runs/Layer (s)	6–26
Circle Runs/ Layer	11
Melt Bead Diameter (mm)	9

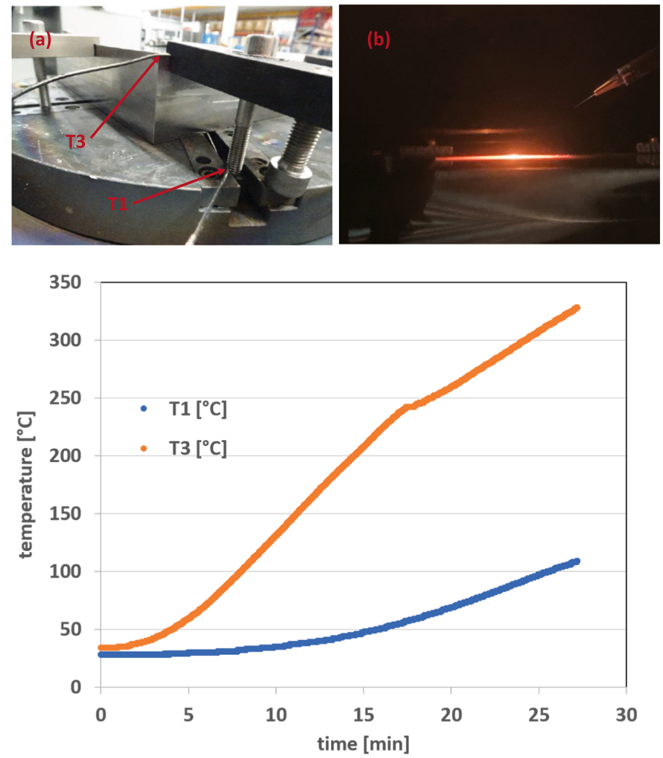

Fig. 5. (a) Locations of thermocouples T1 & T3; (b) side view of pre-heating process; (c) thermocouple T1 & T3 temperatures.

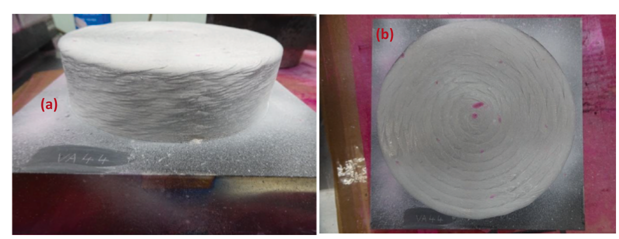

Fig. 6. Dye-penetrant test of distributor cylinder.

Table 4
Description of analysed states of the samples and their post WEBAM treatment.

Component	Sample	Post WEBAM HT	Abbr.
Preliminary Sample 1	PS1	–	AP
Preliminary Sample 2	PS2-1	T1 (750 °C/60 min)	T1
	PS2-2	T1 (750 °C/60 min)	T1
	PS2-3	T1 (750 °C/60 min) &SA (1150 °C/4h) + Q (1050 °C/30 min) + T (750 °C/90 min)	T1 + SA + QT2
Distributor cylinder VA44	CYL-3	–	AP
	CYL-4	SA (1150 °C/4h) + Q (1050 °C/30 min) + T (750 °C/90 min)	SA + QT2
	CYL-3	Q (1050 °C/30 min) + T (750 °C/90 min)	QT2
	CYL-HIP	HIP (100 MPa/1150 °C/4h) + Q (1050 °C/60 min) + T (750 °C/90 min)	HIP + QT3
P92 plate	P92	SA (1150 °C/4h) + Q (1050 °C/30 min) + T (750 °C/90 min)	SA + QT2

Note: AP- as-printed; Q-quenching; T-tempering; SA-solution annealing; HIP-hot isostatic pressing.

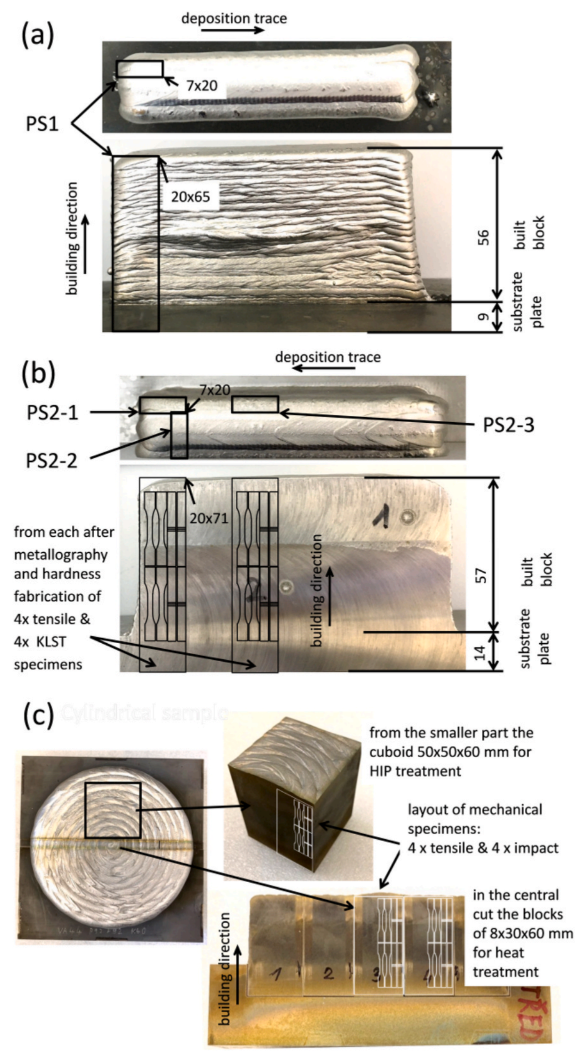

Fig. 7. EDM cutting of samples: (a) PS1, (b) PS2, (c) distributor cylinder sample.

from the central region and one block of larger size was extracted next to this row of blocks by wire-EDM post WEBAM as shown in Fig. 7. The extracted blocks of the distributor cylinder were heat-treated and HIP-treated in following ways:

i) CYL-3: Quenching (1050 °C/30 min) and tempering (750 °C/90 min);
ii) CYL-4: Solution annealing in vacuum (1150 °C/4h) followed by quenching (1050 °C/30 min) and tempering (750 °C/90 min); and
iii) CYL-HIP: HIP treatment (1150 °C/4h/100 MPa/Ar) followed by quenching (1050 °C/60 min) and tempering (750 °C/90 min).

As PS1, CYL-3 was also initially examined in AP condition. A longer austenization time was applied to the HIP-treated block due to its larger size compared to the other block samples. The cooling rates of solution annealing and HIP were 6 °C/min. Depending on the size of samples, the cooling rates of quenching were 25-10 °C/min.

3.3. Material characterization

Metallographic examination was conducted on plate-shaped samples with dimensions (11–30) mm x (65–71) mm x 8 mm, extracted from the components by wire–EDM. Samples for microstructural observations were prepared using a standard metallographic procedure consisting of grinding with SiC sandpapers up to grit P2500, followed by polishing with diamond paste down to 1 μm. After observation in the non–etched condition, the samples were chemically etched by immersing in etchant Villela–Bain for 15 s at room temperature (RT).

Metallographic observations in both non–etched and etched condition were performed using a light digital microscope Olympus DSX1000. The prior austenite grain (PAG) size was evaluated using image analysis of light microscopy images of the etched state by linear intercept method. The quantification of the defects of WEBAM samples were conducted on the extracted blocks of samples in non-etched state. From each state, whole area of the extracted block of built material (of the sample) was examined with a threshold level of 10 μm at 280x magnification, which covered the image area of 0.96 mm^2. For each sample, different number of images were evaluated depending on the evaluated area. For example, analysis of PS2-2 sample in T-orientation with the evaluated area of 682 mm^2 was carried out on 782 images. Defect density was aggregated across the evaluated area (built area) of the sample and its value was calculated as number of defects per area evaluated. The microstructures were also examined by means of scanning electron microscope (SEM-LYRA 3 XMH FEG/SEM, Tescan, Czech Republic) equipped with energy-dispersive X-ray spectroscopy (EDS) detector (Oxford Instruments, Abingdon, UK) operated with Aztec software. The observations were realized in the secondary electron mode at an acceleration voltage of 20 kV.

Vickers hardness was determined using an instrumented hardness tester (ZHU0.2, Zwick/Roell, Germany) under a load of 49 N (HV5), in accordance with the EN ISO 6507 standard. Line hardness measurements were performed along the height of the metallographic samples, with a spacing of 2 mm between indents.

The mechanical properties were assessed by tensile testing and Charpy impact testing at RT. From each metallography sample, sets of semifinished blocks of four tensile and four miniaturized Charpy impact specimens were subsequently extracted. Both specimen types were oriented along the building direction (height) of the component and arranged in two rows and two columns, as indicated in Fig. 7. For the purpose of tensile testing, round tensile specimens with tread heads (M4), a nominal gauge length of 7.6 mm and a diameter of 2 mm were used. For Charpy impact testing, miniaturized KLST-type Charpy specimens with a nominal cross section 3 mm × 4 mm and length 27 mm having a 1 mm deep V-notch were prepared. The tensile tests were performed at a crosshead speed of 1 mm/min corresponding to strain rate $2x10^{-3}s^{-1}$ using a universal test machine (Z50, Zwick/Roell, Germany) according to the ISO 6892–1 standard [27]. Instrumented Charpy impact tests were conducted using an instrumented impact tester equipped with a 15 J capacity hammer (B5113.303, Zwick/Roell, Germany) and anvil span of 22 mm following the ISO 14556 standard [28].

3.4. Reference material of P92 steel

Conventional P92 steel in the form of a 25 mm thick plate was examined to provide a comparison with the WEBAM-produced components. The plate material was manufactured by hot rolling. The final HT consisted of solution annealing in vacuum (1150 °C for 4 h), followed by quenching (1050 °C for 30 min) and tempering (750 °C for 90 min), corresponding to the same HT condition applied to the WEBAM samples, denoted as SA + QT2. Mechanical properties of the conventional P92 steel were evaluated in the S-direction of the plate, i.e., along the direction of thickness (height).

4. Results

4.1. Preliminary samples (PS1 and PS2)

The results of metallographic analyses of preliminary samples PS1 and PS2 oriented in parallel with the longitudinal direction are shown in

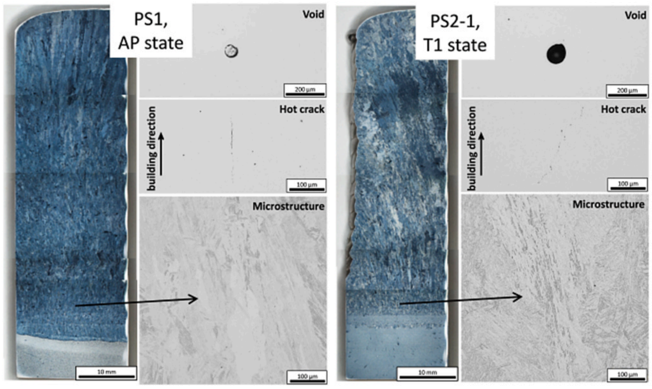

Fig. 8. Metallographic examination of PS1-1 and PS2-1.

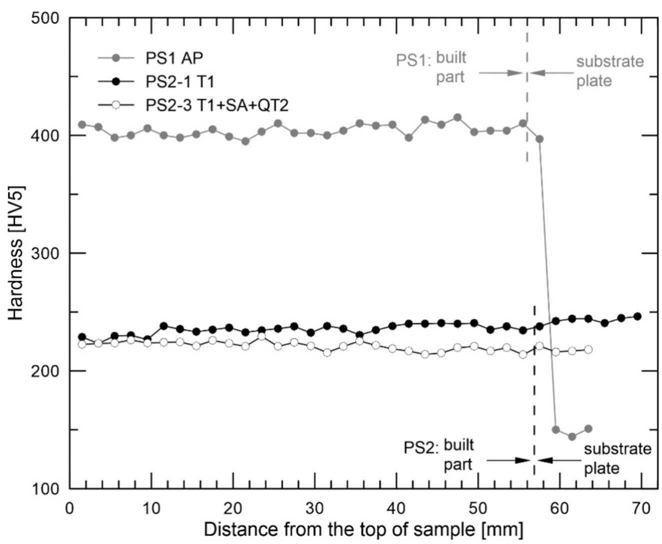

Fig. 9. Hardness profile along the height of preliminary samples.

Fig. 8. The line hardness measurement profiles are shown in Fig. 9. The results of the metallographic evaluation, including the determined PAG size and defect quantification, are summarized in Table 5. As evident in Fig. 8, the weld beads exhibited good penetration into substrate plate of preliminary samples. No discontinuity-type defects, such as cracks or other discontinuities were observed between the substrate and the built part. However, an occurrence of random voids and hot cracks were detected. The longest dimension of the hot cracks was approximately parallel to the building direction of samples.

Sample PS1 in AP state exhibited a martensitic microstructure in the built region, which transitioned to a ferritic microstructure in the substrate. Coarse columnar martensitic grains, preferentially oriented along the building direction, were observed in the built part, with an average PAG size of approximately 1730 μm. The height of the columnar grains increased towards the top of the sample. This grain microstructure formed by columnar grains oriented along the building direction is most likely associated with solidification of built material toward the substrate plate.

The sample PS2-1 in the tempered state (T1) exhibited same type of defects as PS1, random voids and occasional presence of hot cracks. However, the density of hot cracks and their sizes were considerably larger in the transverse sample PS2–2 compared to the longitudinal one. The hot cracks were located more often in the upper part of the built sample with indications of occurrence in mutual distances 6–8 mm in the transversal direction of the sample. Both the built region of the sample and its substrate were composed of tempered martensitic microstructure with distinct change of grain size from fine–grained equiaxial grain in the substrate plate to coarse–grained columnar grains in the built. The average PAG size in the T1 condition of sample PS2 (1681 μm) was comparable to that measured in the AP state of sample PS1 as tabulated in Table 5.

Table 6 summarizes the results of mechanical characterization and average hardness obtained from line hardness measurements in the built region of the samples, excluding the substrate plate. The results of all four mechanical specimens of tensile and impact testing without no exclusions were used to calculate each mean value of characteristic and its standard deviation. Mechanical characterization of sample PS1 was omitted due to the presence of brittle martensitic microstructure. Both tensile and KLST specimens demonstrated fully ductile fracture behaviour. Table 6 also includes the data of conventional P92 steel. The T1 HT, consisting of tempering (750 °C/60 min) provided strength values close to those of conventional P92 steel. However, the uniform elongation values (A_g) and especially the total elongation values (A) were lower than those of the reference. Note that, for P92 steel, a minimum A value of 20 % is prescribed. In addition, a slant fracture surface was observed in PS2-1 tensile specimens, which differs from the characteristic cup-

Table 5
Results of metallography and image analyses of PAG size in etched state and defect quantification in non–etched state.

Sample	State	Orientation	PAG [μm]	Area evaluated [mm^2]	Hot Cracks <10–50 um>		Hot Cracks >50 um		Voids <10–50 um>		Voids >50 um	
					l [μm]	ρ [mm^{-2}]	l [μm]	ρ [mm^{-2}]	d [μm]	ρ [mm^{-2}]	d [μm]	ρ [mm^{-2}]
PS1	AP	L	1730 ± 457	1286	21 ± 12	0.002	62 ± 94	0.001	22 ± 13	0.025	69 ± 70	0.030
PS2-1	T1	L	1681 ± 512	1187	18 ± 13	0.001	54 ± 76	0.001	19 ± 16	0.031	78 ± 49	0.019
PS2-2	T1	T	1763 ± 489	682	25 ± 10	0.029	115 ± 81	0.007	23 ± 13	0.029	100 ± 39	0.027
PS2-3	T1 + SA + QT2	L	245 ± 79	1107	22 ± 10	0.002	73 ± 81	0.002	24 ± 15	0.025	95 ± 34	0.028
CYL-3	AP	R	1578 ± 638	1293	24 ± 13	0.013	198 ± 210	0.009	23 ± 11	0.037	113 ± 96	0.011
CYL-4	QT2	R	234 ± 101	1323	26 ± 11	0.015	126 ± 183	0.004	22 ± 10	0.031	90 ± 97	0.014
CYL-3	SA + QT2	R	263 ± 86	1358	24 ± 15	0.012	152 ± 163	0.012	25 ± 18	0.048	124 ± 109	0.009
CYL-HIP	HIP + QT3	R	258 ± 108	1342	24 ± 13	0.006	–	–	19 ± 8	0.003	118 ± 58	0.004
P92	SA + QT2	T	84 ± 29	–	–	–	–	–	–	–	–	–

Note: l - length of hot crack (the longest dimension), ρ - areal density of defects (number of defects per mm^2), ± means the standard deviation.

Table 6
Average values of mechanical characteristics of preliminary samples and the samples of distributor cylinder

Sample	PS1	PS2-1	PS2-3	P92	CYL-3	CYL-4	CYL-3	CYL-HIP
State	AP	T1	T1 + SA + QT2	SA + QT2	AP	QT2	SA + QT2	HIP + QT3
HV5	404 ± 5	235 ± 4	222 ± 4	230 ± 3	413 ± 4	224 ± 4	223 ± 3	215 ± 2
YS [MPa]	–	613 ± 20	541 ± 4	609 ± 1	–	555 ± 7	549 ± 7	531 ± 3
UTS [MPa]	–	751 ± 19	707 ± 2	747 ± 2	–	711 ± 2	702 ± 2	698 ± 1
A_g [%]	–	6.2 ± 0.7	8.8 ± 0.3	7.2 ± 0.2	–	8.0 ± 0.5	7.7 ± 0.5	8.7 ± 0.2
A [%]	–	17.7 ± 3.4	28.5 ± 3.0	24.0 ± 2.0	–	23.9 ± 0.4	23.7 ± 0.5	27.0 ± 2.0
KV [J]	–	7.2 ± 0.3	8.4 ± 0.1	6.5 ± 0.8	–	8.5 ± 0.3	8.3 ± 0.4	8.3 ± 0.2

Note: ± means the standard deviations.

cone fracture typical of P92 steel. Despite this, the built material demonstrated slightly higher impact energy (KV) of 7.2 J than its conventional counterpart (6.5 J) as shown in Table 6. The observed difference in deformation and fracture behaviour of the built material are attributed to its specific grain microstructure composed of columnar grains. HT by the tempering process itself (T1) was not found to be suitable for the properties of WEBAM produced material. Therefore, HT consisting of solution annealing followed by quenching & tempering (denoted as T1 + SA + QT2) was consequently applied to the PS2-3 sample. This additional HT led to more uniform tempered martensitic microstructure in both the substrate and the built region of the sample. The PAGs of T1 + SA + QT2 state became more equiaxial and were refined to about 245 μm. Comparing to the T1 condition, a slight decrease in hardness from 235 to 222 HV5 was observed (Table 6). At the same time, both A_g and A improved significantly to 8.8 % and 28.5 %, respectively, exceeding the values measured for the conventional P92 steel. On the other hand, the yield strength (YS) and ultimate tensile strength (UTS) decreased to 541 MPa and 707 MPa, respectively. The

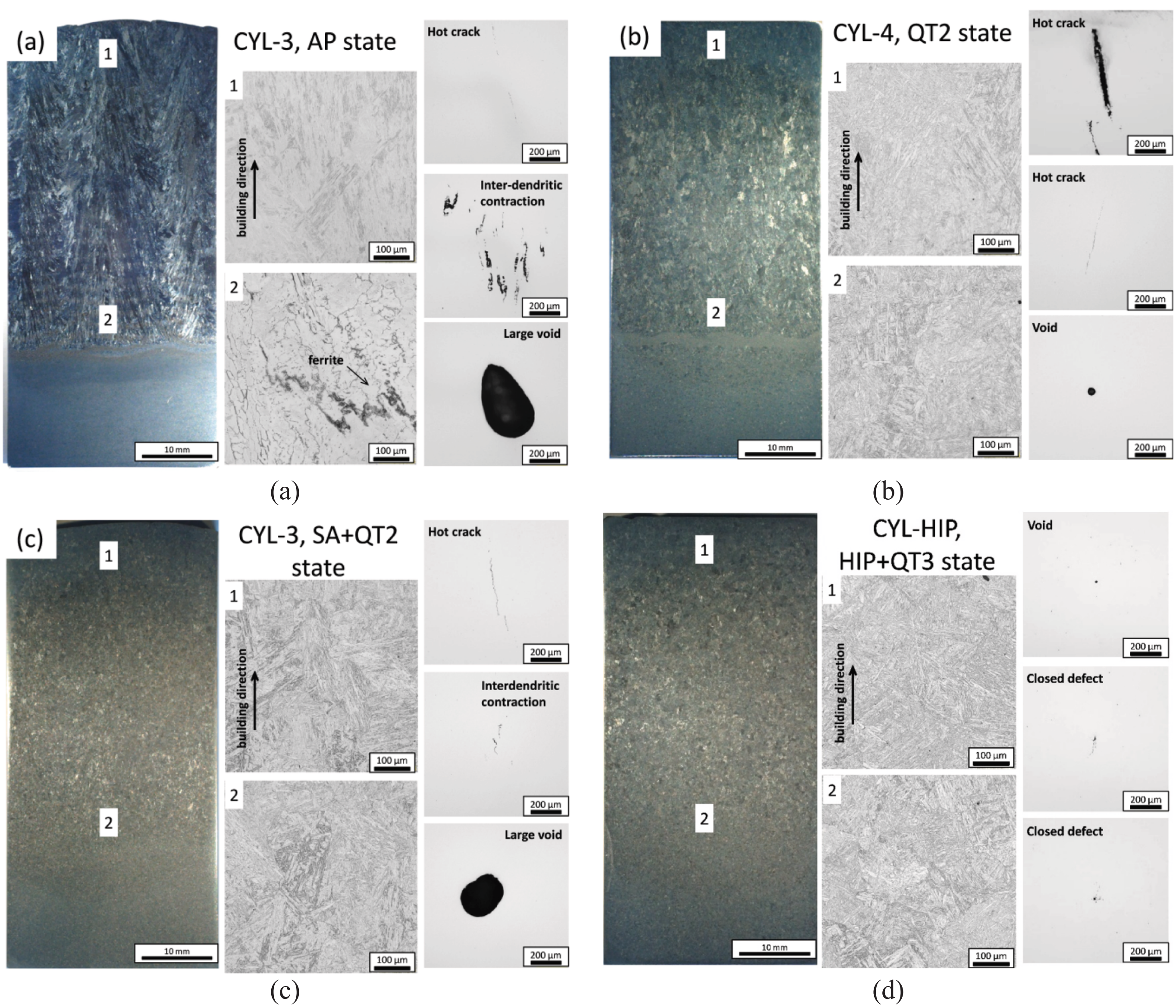

Fig. 10. Metallographic examination of distributor cylinder samples.

relatively coarse PAG size in the built material is considered to be the main reason for the lower strength compared to the conventional material, which has a grain size of approximately 84 μm. The improved deformation behaviour in the T1 + SA + QT2 condition was also reflected in its impact energy which demonstrated an increase to 8.4 J.

4.2. Distributor cylinder

The results of metallographic analyses of cylindrical samples are shown in Fig. 10 and the line hardness measurement profiles are shown in Fig. 11. No discontinuity defects like cracks or other discontinuities were observed between the substrate and the built material in non-etched conditions for any of the examined sections of the cylindrical sample.

In the AP condition, represented by sample CYL-3, the built material exhibited a defect density comparable to that observed in the transversely oriented preliminary sample PS2-2. However, a notable difference between the cylindrical and preliminary samples was the larger size of individual defects, particularly voids and hot cracks. The most common types of defects were voids with random distribution within the sample. The densities of small voids (10–50 μm) and large voids (>50 μm) were 0.037 mm^{-2} and 0.011 mm^{-2}, respectively. Hot crack-type defects were less common and were mostly concentrated in the upper part of the built sample. Occasionally, the mutual spacing of the individual hot cracks in distances of 6–8 mm in horizontal direction was observed. The densities of short hot cracks (10–50 μm) and long hot cracks (>50 μm) were 0.013 mm^{-2} and 0.009 mm^{-2}, respectively as shown in Table-5. A single large inter-dendritic contraction defect with a diameter of approximately 874 μm was detected in this sample as shown in Fig. 10a. Because no other large inter dendritic contractions were detected in other cylindrical samples, this type of the defect was considered rare. The dominant orientation of defect type of hot cracks – either as individual long discontinuities or as strings of shorter discontinuities – were nearly parallel to the build direction of the sample. SEM observations combined with local EDS chemical analysis of hot cracks are presented in Fig. 12. The random presence of MnS particles (Fig. 12a) and Cr, W, Mo, Nb, V rich carbides were detected inside the discontinuities forming the hot cracks (Fig. 12b). In general, the regions with hot cracks showed locally increased concentrations of Cr and O compared to the surrounding matrix, indicating chemical heterogeneity in these areas (Fig. 12d). No exceptional element content when compared to the matrix, was detected inside the large inter dendritic contraction described above (Fig. 12c).

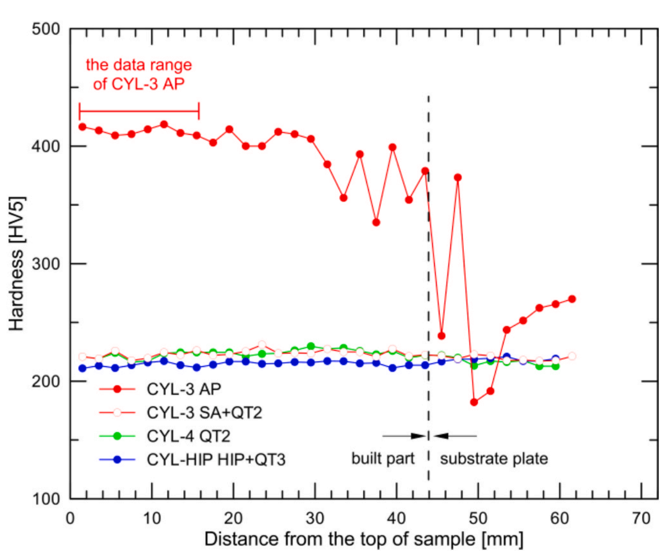

Fig. 11. Hardness profile along the height of metallography samples of the distributor cylinder.

In etched condition, AP state contained martensitic microstructure in 1/3 of the built height. From approximately 2/3 of the height of the sample, the amount of ferrite continuously increased in the direction of the interface with substrate plate. This trend is visible on the hardness profile in Fig. 11. The average hardness of the top 1/3 of the built sample is 413 HV5 which corresponds to the hardness of martensite phase of Grade 92 steel. The interface between the built material and substrate plate for cylindrical samples was located approximately at the distance of 44 mm from the top of the sample. Minimal hardness 182 HV5 was observed in the distance of 50 mm from top of the sample, thus, approximately at a depth 6 mm of the substrate plate. Further, the hardness slightly increased with the increasing depth of the substrate. This observation is consistent with the fact that the weld beads penetrated into substrate plate up to the depth of 3 mm. The grain microstructure in the built region consisted of large columnar grains with a height of about 2.5 mm, preferentially oriented along the building direction of the sample. The grain size increased toward the top of the sample, and an average PAG size of 1681 μm was determined.

Sample CYL–4 in the QT2 state exhibited same type of defects as sample CYL-3. After QT2 HT, the built part of the sample and the substrate were formed by tempered martensitic microstructure with distinct change of grain size from fine–grained part of the substrate to coarse–-grained part of the built. Between the built material and the substrate, a band with fine grains was observed resembling the heat affected zone (HAZ) similar to that of the fusion welding. The PAG of the built material of QT2 state had equiaxial shape and its size was refined to 234 μm.

Table 6 shows the results of mechanical characterization and the average line hardness in the built part of the sample excluding the substrate plate for CYL-4. The QT2 state provided uniform hardness profile with the average value 224 HV5. Both tensile and KLST specimens of all the states of HTs and HIP treatment of cylindrical samples demonstrated fully ductile fracture behaviour. The YS and UTS were about 54 MPa and 35 MPa lower than for conventional P92 steel, respectively. On the contrary, A_g was about 0.8 % lower and A was nearly the same as for the conventional P92 steel. No adverse effect of the defects of built material on its deformation and fracture behaviour in QT2 state was observed. The difference in tensile properties here can be explained by difference in grain size which is larger than for the reference. The built material in QT2 state demonstrated the impact energy 8.5 J which is about 2 J higher than that of the conventional material.

The sample CYL–3 in the SA + QT2 state in non–etched condition exhibited same type of defects as before HT. After HT, both the built part and substrate plate were composed of tempered martensitic microstructure. The PAGs of built material were dominantly equiaxial with uniform grain size distribution throughout the height of the sample with an average size 263 μm and the PAGs of substrate plate coarsened to about 80 μm. Thus, smooth transition of grain size at the interface of the built material and substrate plate was achieved. The hardness profile with regular values along the height of the sample with the average value 223 HV5 of its built part was obtained. The tensile and impact properties of SA + QT2 state were close to those of QT2 state.

The CYL-HIP sample was characterized after HIP treatment subsequently followed by quenching and tempering, i.e., in the state denoted HIP + QT3 state. The metallographic analysis in non-etched condition revealed significant decrease in densities and sizes of both types of defects compared to other cylindrical samples. The large defects with compact shape were classified as the defects type of large voids (shown in Fig. 10d). The shape of these defects suggests that these are the remains of the discontinuities compacted by closure of larger hot cracks or voids by the effect of isostatic pressure. The density of short hot cracks (10–50 μm) decreased approximately to half value of 0.006 mm^{-2}, while their average length remained unchanged (24 μm), however, no long hot cracks (>50 μm) were detected. The density of the small voids (10–50 μm) dropped nearly by the level of order to 0.003 mm^{-2} and their average diameter slightly decreased to 19 μm. The density of large voids (>50 μm) decreased approximately to one-third to 0.003 mm^{-2} as

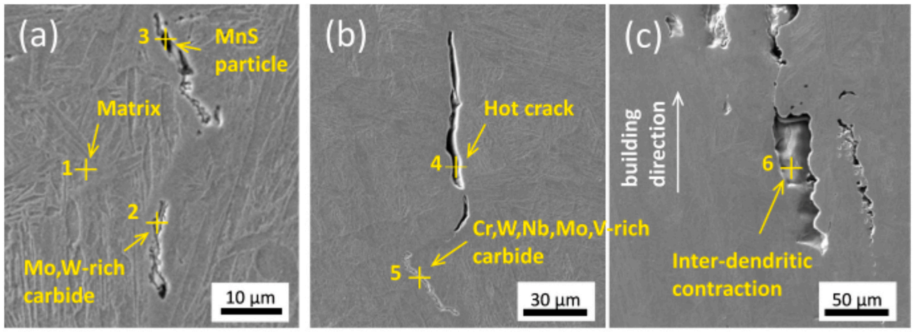

(d)

Site	Fe	Cr	W	Mn	Mo	Si	Ni	V	Nb	S	C	O
	wt.%											
1	86.9	9.0	2.2	0.5	0.4	0.4	0.1	0.2	0.1	0.1	0.0	0.0
2	83.3	9.6	2.4	0.5	1.0	0.5	0.1	0.2	0.0	0.0	2.6	0.0
3	72.2	15.1	0.6	4.5	0.3	0.1	0.2	0.4	0.0	6.2	0.0	0.5
4	85.0	11.3	1.7	0.4	0.5	0.3	0.1	0.2	0.1	0.0	0.0	0.4
5	65.5	17.4	4.1	0.3	1.8	0.3	0.1	0.7	4.4	0.0	5.4	0.0
6	87.4	9.6	1.5	0.4	0.2	0.4	0.1	0.1	0.0	0.1	0.0	0.0

Fig. 12. SEM observation & results of point EDS analysis of hot cracks of sample CYL-3 in AP state: a) strings of particles at the hot cracks, b) hot crack and string of particles c) large inter–dendritic contraction, d) chemical composition measured at indicated sites.

shown in Table 5. The thermal history of the sample CYL-HIP in the conditions of treatment HIP + QT3 nearly corresponds to the conditions of the state SA + QT2 of sample CYL–3 with the only difference of longer austenization time of 60 min. The PAGs of built material of the CYL-HIP sample were dominantly equiaxial with average size 258 µm thus, similar to that of the SA + QT2 condition. The PAGs of substrate plate coarsened to about 100 µm. Also, a smooth transition of grain size at the interface between built material and substrate plate was observed and the average hardness value of the HIP + QT3 state decreased to 215 HV5. The YS and UTS were about 78 MPa and 49 MPa lower than that of conventional P92 steel, respectively. Better deformation properties of tensile testing and the impact energy than that of conventional steel were also achieved as the A_g, A and KV were 1.5 %, 3.0 % and 1.8 J higher than the reference values, respectively.

5. Discussions

5.1. Discussion of results

Preliminary and cylindrical samples derived from the deposition process had the microstructure in the form of columnar grains. The main difference between the samples was their deposition trace. For preliminary samples, with the linear deposition trace, the anisotropy of distribution of hot crack-type defects was observed. The longitudinally oriented samples contained lower density of hot cracks than the transversally oriented sample. In contrast, no anisotropy in hot cracks was observed in the cylindrical samples with circular deposition trace, where no single longitudinal deposition orientation exists. Thus, the deposition trace is an important factor affecting the anisotropy of the defects in printed material and thus, its mechanical properties. Similar conclusion had been drawn also for the wire arc additive manufactured (WAAM) blocks of nickel-based Alloy 718 [29].

The main microstructural difference between the preliminary samples and the cylindrical samples in the AP state was the presence of ferrite in the lower region of the built part of the cylindrical sample. The occurrence of ferrite, together with its gradually increasing fraction toward the substrate plate, indicates a different cooling rate during the deposition process in the cylindrical sample compared to the smaller preliminary samples. This suggests that the lower portion of the cylindrical build experienced a self-tempering effect associated with preheating of the substrate during deposition. However, apart from the difference in phase composition, no other apparent microstructural differences between the preliminary and cylindrical samples attributable to the preheating effect were observed.

The voids and hot cracks observed in the WEBAM samples are solidification-induced defects of the deposition process. The hot cracks – either in the form of long individual discontinuities or strings of shorter discontinuities – were aligned with the building direction of the sample. These hot cracks were most likely located near inter-bead regions, which can be susceptible to microstructural heterogeneities and defect formation. In some cases, hot cracks appeared periodically spaced at approximately 6–8 mm in the horizontal direction of the samples. The EDS analysis in SEM revealed the presence of the particles of MnS and Cr, W, Mo, Nb, V rich carbides inside the strings of shorter hot cracks. The MnS particles have low melting point and are usually created at the locations which solidify last. The presence of the Cr, W, Mo, Nb, V rich carbides inside the strings of hot cracks can be explained by the chemical heterogeneity of these regions compared the surrounding matrix of the steel. These observations suggest that hot crack-type defects form due to the presence of inter-granular liquid films and resulting melt-pool solidification processes associated with hot cracking [28]. The main differences between the defects observed in the preliminary samples and those in the cylindrical samples are the anisotropic distribution of defects in the preliminary samples and the larger size of defects (>50 µm) in the cylindrical samples. Different deposition trace and size of printed volume vary condition of solidification process at local site and modify the conditions supporting the creation of inter–granular liquid films connected with hot cracking [28]. The larger defects observed in the cylindrical samples are most likely related to the different deposition trace applied and the scale effect associated with larger deposited volume.

No evident detrimental effect of hot cracks or voids in the built material on the deformation and fracture behaviour of either the preliminary or cylindrical samples were observed. This may be explained by several factors: (i) the relatively low density of defects, (ii) the small size and limited number of mechanical specimens tested, and (iii) the

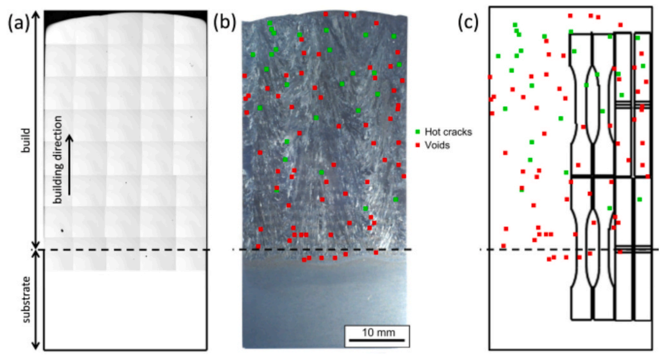

Fig. 13. The analysis of defects of the cylindrical sample CYL3 in SA + QT2 state: a) the quantified area of the sample in non-etched state, b) the sample in the etched state with the location of observed defects, c) layout of the defects with location of the mechanical specimens.

orientation of the specimens along the building direction of the samples. Fig. 13 shows an overview of the metallographic samples together with the spatial distribution of defects and the locations of the extracted mechanical specimens. It can be seen that the mechanical specimens were taken from regions where defects were present. However, metallographic analysis reflects only the areal distribution of defects in the observation plane, and the average defect density was relatively low. For example, the cumulative defect density measured in sample CYL-3 in the QT2 state was 0.064 mm^{-2}, corresponding to an average area per defect of approximately 15.6 mm^2. The used miniature specimens covered only limited sampling volume of the material. Next, relatively low number (4 pieces) of each type of specimens were used. Another possible reason of good results of mechanical testing could be chosen orientation of the specimens along the building direction which reduced their sensitivity to hot cracks-type defects which itself were predominantly oriented parallel to this direction. The specimens oriented in transversal direction located in the upper part of the printed builds would likely be more sensitive to the observed hot cracks-type defects. Due to this, the applied mechanical testing has limited reliability regarding the sampling of the defects observed in the deposited material. Nevertheless, the mechanical results of WEBAM samples indicate good deformation and fracture behaviour of the matrix of deposited steel. At the same time an option that the effect of observed defects on deformation and fracture behaviour of the steel is only limited cannot be excluded.

The most suitable HT for the WEBAM-produced material was found to be solution annealing followed by quenching and tempering. This treatment normalizes the coarse-grained microstructure of both the deposited material and the substrate plate. However, reduction of defects in the deposited material requires the application of HIP. It was demonstrated that these defects can be effectively mitigated by HIP treatment performed at condition 100 MPa/1150 °C/4h. Proposed HT combining solution annealing, quenching and tempering led to microstructures of tempered martensite with relatively coarse PAG size of about 250 μm. These microstructural states provided yield strength and ultimate tensile strength on the level of 550 MPa and 700 MPa, respectively. The conventional P92 steel with the average PAG size of 84 μm achieved YS and UTS of 609 MPa and 747 MPa, respectively. The differences between strength properties of the heat–treated specimens can be explained by slight variation of PAG sizes and derived microstructural features of tempered martensite [30].

5.2. Application of WEBAM for monoblock components manufacturing

To address the challenges associated with the reference EU DEMO design and manufacturing, a modular Monoblock BB design has been proposed for the European DEMO Helium-Cooled Pebble Bed (HCPB) concept (shown in Fig. 1 and 14). As described earlier in the

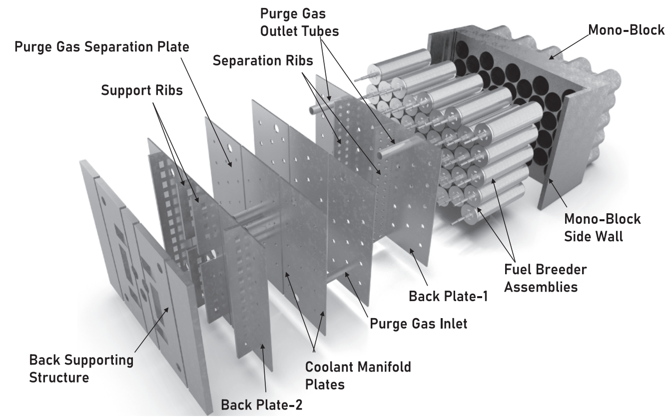

Fig. 14. Exploded view of an assembled KIT Monoblock BB section [3].

introduction, a Monoblock BB refers to a BB architecture in which the FW and the BZ structure are constructed out of a single solid block. To assemble such a BB, FBA are inserted in the rear circular holes of the forged, solid machined monoblock sequentially and in further steps, each part is aligned and assembled using TIG/EB Welding to the forged solid machined monoblock in a similar approach as shown in Fig. 14 [3]. Manufacturing a BB with this approach simplifies the fabrication by reducing the total number of weld joints and by significantly reducing welds at the plasma facing front region and enhances robustness against neutron irradiation and thermal loads. For example, in the reference HCPB BB design, the FW and the BZ were separate components which needed to be welded to one another [1], however, in the Monoblock BB, such welding is not needed. Further, this design can be manufactured using a cost-effective, scalable process and qualified (both design and manufacturing) as per the requirements of RCC-MRx: N2Rx [3].

Although preliminary, the present investigations provide a positive outlook, firstly regarding WEBAM as a promising manufacturing technique with unique advantages, and further regarding the feasibility of scaling the manufacturing process to specimen sizes larger than the distributor cylinder. As informed in earlier section, in the WEBAM process, a maximum deposition rate of 3.41 kg/h has been achieved which can be further increased by increasing the feed wire thickness, the EB intensity and proces parameter optmisation. Further, the base plate of this machine is capable to move in 3-axes and can rotate and tilt which aids in manufacturing complex geometries. In addition, depending on the manufacturing geometry, different tracing routes of the beam (linear tracing for preliminary samples and circular tracing for distributor cylinders) has been achieved. Also, the EB technology has unique capability to pre-heat the base plate already installed, in high vacuum just before the deposition process. Therefore, from manufacturing perspective, WEBAM is suitable for large-scale components manufacturing. However, based on the present findings, increasing build dimensions and deposited volume substantially modifies heat accumulation, cooling rates, and the overall thermal history of the component which, in turn, influences microstructural evolution and defect formation, further highlighting the need for multiple additional systematic scaling studies, with progressively larger build sizes, together with careful consideration of build geometry and optimization of process parameters.

Though both Grade 92 steel and Eurofer97 has similar weldability behaviour, there exists certain limitations with respect to the transferability of WEBAM process and post-processing parameters (HT and HIP parameters) to Eurofer97 and needs further investigation through additional studies. For this, firstly, production of Eurofer97 wires of appropriate diameter will be mandatory. In addition, the time–temperature transformation and tempering response of Eurofer97 will be different from Gr.92 Steel, hence, process and post-process parameter optimization derived on Grade 92 would need certain minor adjustments when applied on Eurofer97. For example, as reported by Bonk *et al.* [16] for SLM of Eurofer97, to reduce the residual random porosities after the process, following post processing was done in AP state: HIP (1000 °C/100Mpa/2.5 hrs) followed by austenization at 980 °C for 30 mins with quenching in air and with further tempering at 750 °C for 2 hrs. When compared to the post-processing parameters utilized for Grade 92 steel in the present investigation, it is evident that the parameters are not significantly different. Bonk *et al.* also reported that for Eurofer97 after SLM possessed peculiar anisotropic, bimodal and partial ferrite microstructure and only after HT and HIP, it transformed to a fully equiaxed martensitic microstructure similar to that of a conventional Eurofer97 which is also witnessed for Grade 92 steel in the present investigation.

6. Conclusion

The present study provides a preliminary assessment of WEBAM as a potential AM route for Monoblock HCPB BB components, with experimental findings providing insights into the deposition scale effects on the microstructure, defect characteristics, and mechanical properties Particular attention was given to the evolution of scale-dependent manufacturing defects and to the effectiveness of post-WEBAM HT and HIP in mitigating these observed defects. For this purpose, WEBAM samples of two different sizes were deposited on P92 substrates and further metallographic analyses, hardness measurements, and mechanical testing, including tensile and Charpy impact tests were performed to assess the properties of the AM material relative to those of the Grade 92 base material.

A key strength of the present study is the systematic experimental assessment of WEBAM across two deposition scales and multiple post-processing routes, combining microstructural characterization and defect quantification with mechanical property evaluation through hardness, tensile, and impact testing. Comparison with reference Grade 92 steel subjected to comparable HT further enables the interpretation of AM-induced differences in material characteristics and mechanical performance. This provides a good initial experimental basis for assessing the suitability of WEBAM for the fabrication of Monoblock HCPB BB components.

Following are the key findings of the present study:

a) In AP state, samples from larger build sizes showed signs of self-tempering effect associated with preheating of the substrate during deposition;
b) Samples from smaller build sizes showed anisotropic defect distribution whereas samples from larger build sizes showed larger sizes of defects;
c) Solution annealing in combination with quenching and tempering has been found to be most suitable post-AM HT for improving the microstructure and mechanical performance;
d) However, HIP treatment has been found necessary for effective mitigation of defects.

These findings demonstrate that WEBAM can deliver promising microstructural and mechanical properties of bulk Grade 92 material when combined with suitable post-processing HT and HIP. WEBAM has been found suitable for large-scale component manufacturing due to its ability to reach relatively high deposition rate and its capability for in-vacuum preheating, which facilitate the deposition of large build volumes while providing greater control over the thermal conditions during fabrication. However, the scale-dependent differences observed in the present study indicate that increasing build dimensions and deposited volume modifies heat accumulation, cooling rates, and the overall thermal history of the component further affecting the microstructural evolution and defect formation. Therefore, the transition toward large-scale WEBAM will require numerous additional systematic scaling studies, with progressively larger build sizes, together with careful consideration of build geometry and optimization of process parameters. Furthermore, the transferability of WEBAM processing and post-processing parameters from Grade 92 steel to Eurofer97 will require material-specific adjustments, necessitating further investigation.

CRediT authorship contribution statement

Gaurav Verma: Writing – review & editing, Writing – original draft, Visualization, Resources, Methodology, Conceptualization. **Luděk Stratil:** Writing – review & editing, Writing – original draft, Visualization, Methodology, Investigation, Formal analysis, Conceptualization. **Jörg Rey:** Writing – review & editing, Supervision, Resources, Project administration, Conceptualization. **Bernd Baufeld:** Writing – review & editing, Visualization, Investigation, Formal analysis, Data curation. **Martin Petersen:** Writing – review & editing, Visualization, Investigation. **Stephen Fischer:** Writing – review & editing, Resources. **Heiko Neuberger:** Writing – review & editing, Visualization. **Francisco A. Hernández:** Writing – review & editing, Resources, Funding acquisition. **Jarir Aktaa:** Writing – review & editing.

Declaration of competing interest

The authors declare the following financial interests/personal relationships which may be considered as potential competing interests: Gaurav Verma reports financial support was provided by European Consortium for the Development of Fusion Energy. If there are other authors, they declare that they have no known competing financial interests or personal relationships that could have appeared to influence the work reported in this paper.

Acknowledgments

This work has been carried out within the framework of the EUROfusion Consortium, funded by the European Union via the Euratom Research and Training Programme (Grant Agreement No 101052200-EUROfusion). Views and opinions expressed are however those of the author(s) only and do not necessarily reflect those of the European Union or the European Commission. Neither the European Union nor the European Commission can be held responsible.

Data availability

Data will be made available on request.

References

[1] F.A. Hernández, P. Arena, L.V. Boccaccini, I. Cristescu, A.D. Nevo, P. Sardain, G. A. Spagnuolo, M. Utili, A. Venturini, G. Zhou, The European DEMO helium cooled pebble bed breeding blanket: design status at the conclusion of the pre-concept design phase advancements in designing the DEMO driver blanket system at the EU DEMO pre-conceptual design phase: overview, challenges and opportunities, J. Nucl. Eng. 4 (2023) 565–601, https://doi.org/10.3390/jne4030037.

[2] G. Zhou, F.A. Hernández, P. Pereslavtev, B. Kiss, A. Retheesh, L. Maqueda, J. H. Park, The European DEMO helium cooled pebble bed breeding blanket: design status at the conclusion of the pre-concept design phase, Energies 16 (14) (2023) 5377, https://doi.org/10.3390/en16145377.

[3] G. Verma, J. Rey, F.A. Hernández, H. Neuberger, M. Zmitko, G. Aiello, M. Rieth, J. Aktaa, Comparative assessment of RAFM steel first wall structural manufacturing technologies for fusion breeding blankets: from ITER TBM to DEMO, Results Eng. (2026) 112490, https://doi.org/10.1016/j.rineng.2026.112490.

[4] H. Li, X. Fu, L. Zhang, Y. Zhang, L. Jiang, Z. Pu, A review of the latest developments in the field of additive manufacturing techniques for nuclear reactors, Crystals 12 (7) (2022) 918, https://doi.org/10.3390/cryst12070918.

[5] A. Sasi, M. Srivastava, K. Dash, Role of additive manufacturing in developing functionally graded materials for nuclear applications, Front. Nucl. Eng. 4 (2025), https://doi.org/10.3389/fnuen.2025.1603437.

[6] Oak Ridge National Laboratory https://www.ornl.gov/news/additively-manufactured-components-ornl-headed-tva-nuclear-reactor, 2020 (accessed 10 Nov 2025).

[7] IAEA https://www.iaea.org/bulletin/embracing-the-promise-of-additive-manufacturing-for-advanced-nuclear-reactors, 2023 (accessed 11 Nov 2025).

[8] AMFG Autonomous Manufacturing https://amfg.ai/2024/01/18/will-additive-manufacturing-power-the-evolution-of-nuclear-energy, 2024 (accessed 11 Nov 2025).
[9] AFCEN, RCC-M 2024: Design and Construction Rules for Mechanical Components of PWR Nuclear Islands (2024).
[10] ASME BPVC Section III 2025: Rules for Construction of Nuclear Facility Components-Division 1-Subsection NC-Class 2 Components (2025).
[11] ASME BPVC Section IX 2025: Welding, Brazing, and Fusing Qualifications (2025).
[12] AFCEN, RCC-MRx 2025: Design and Construction Rules for Mechanical Components of Nuclear Installations: Advanced, Research and Fusion Reactors (2025).
[13] H. Neuberger, F.A. Hernández, J. Rey, S. Bonk, M. Rieth, J. Koch, B. Schmalisch, O. Müller, K.U. Volker, D. Volker, S. Leyh, R. Niewöhner, A. Brenner, Fabrication of HCPB breeding blanket components using the additive manufacturing processes of selective laser melting and cold spray, Fus. Eng. Des. 160 (2020) 112026, https://doi.org/10.1016/j.fusengdes.2020.112026.
[14] H. Neuberger, F.A. Hernández, S. Ruck, F. Arbeiter, S. Bonk, M. Rieth, L. Stratil, O. Müller, K.U. Volker, Advances in additive manufacturing of fusion materials, Fus. Eng. Des. 167 (2021) 112309, https://doi.org/10.1016/j.fusengdes.2021.112309.
[15] H. Neuberger, J. Rey, F.A. Hernández, S. Ruck, C. Koehly, L. Stratil, R. Niewöhner, A. Felde, Evaluation of conservative and innovative manufacturing routes for gas cooled test blanket module and breeding blanket first walls, Fus. Eng. Des. 146 (2019) 2140–2143, https://doi.org/10.1016/j.fusengdes.2019.03.124.
[16] S. Bonk, H. Neuberger, D. Beckers, J. Koch, S. Antusch, M. Rieth, Additive manufacturing technologies for EUROFER97 components, J. Nucl. Mater. 548 (2021) 152859, https://doi.org/10.1016/j.jnucmat.2021.152859.
[17] D. Svetlizky, M. Das, B. Zheng, A.L. Vyatskikh, S. Bose, A. Bandyopadhyay, J. M. Schoenung, E.J. Lavernia, N. Eliaz, Directed energy deposition (DED) additive manufacturing: physical characteristics, defects, challenges and applications, Mater. Today 49 (2021) 271–295, https://doi.org/10.1016/j.mattod.2021.03.020.
[18] Sciaky Press Releases https://www.sciaky.com/news/press-releases/ebam-surpasses-40-lb-metal-deposition-rate, 2024 (accessed 12 Nov 2025).
[19] K.M. Taminger, R.A. Hafley, Electron beam freeform fabrication for cost effective near-net shape manufacturing, NATO/RTO AVT 139 (2006) 11–16. https://ntrs.nasa.gov/api/citations/20080013538/downloads/20080013538.pdf.
[20] P. Wanjara, K. Watanabe, C. de Formanoir, Q. Yang, C. Bescond, S. Godet, M. Brochu, K. Nezaki, J. Gholipour, P. Patnaik, Titanium alloy repair with wire-feed electron beam additive manufacturing technology, Adv. Mater. Sci. Eng. (2019) 3979471, https://doi.org/10.1155/2019/3979471.
[21] K. Osipovich, K. Kalashnikov, A. Chumaevskii, D. Gurianov, T. Kalashnikova, A. Vorontsov, A. Zykova, V. Utyaganova, A. Panfilov, A. Nikolaeva, A. Dobrovolskii, V. Rubtsov, E. Kolubaev, Wire-feed electron beam additive manufacturing: a review, Metals 13 (2) (2023) 279, https://doi.org/10.3390/met13020279.
[22] J. Fuchs, C. Schneider, N. Enzinger, Wire-based additive manufacturing using an electron beam as heat source, Weld WORLD 62 (2018) 267–275, https://doi.org/10.1007/s40194-017-0537-7.
[23] ASME BPVC Section II 2025: Materials Part-A Ferrous Materials Specifications (2025).
[24] L. Forest, J. Tosi, A.L. Puma, O. Doyen, N. Thomas, M. Simon-Perret, M. Zmitko, The European ITER Test Blanket Modules: Fabrication R&D progress for HCLL and HCPB, Fus. Eng. Des. 136 (2018) 1408–1416, https://doi.org/10.1016/j.fusengdes.2018.05.026.
[25] B. Baufeld, T. Dutilleul, Electron_Beam_Additive_Manufacturing_at_the_Nuclear_AMRC, Elektronika Ir Elektrotechnika 51 (5–6) (2016) 25–31. https://www.researchgate.net/publication/303994434_EE_562016_Electron_Beam_Additive_Manufacturing_at_the_Nuclear_AMRC.
[26] Voestalpine Welding Shop https://weldingshop.voestalpine.com/DE/de/documents/download/ZG9jXzIwMjAwOTIyX0RhdGVuYmxhdHQgVEhFUk1BTklUIE1UUyA2MTYgU3RhYmVsZWt0cm9kZS5wZGZ8T25saW5lfHZvZXN0UHJvZHVjdENhdGFsb2cwOTIw?inline=true, 2023 (accessed 14 Nov 2025).
[27] ISO 6892-1:2019 - Metallic materials - Tensile testing - Part 1: Method of test at room temperature (2019).
[28] ISO 14556:2023 - Metallic materials - Charpy V-notch pendulum impact test - Instrumented test method (2023).
[29] C.E. Seow, J. Zhang, H.E. Coules, G. Wu, C. Jones, J. Ding, S. Williams, Effect of crack–like defects on the fracture behaviour of Wire-Arc Additively Manufactured nicke–base Alloy 718, Addit. Manuf. 36 (2020) 101578, https://doi.org/10.1016/j.addma.2020.101578.
[30] T. Karthikeyan, M.K. Dash, R. Ravikirana, S.P. Mythili, A. Selvi, S.S. Moitra, Effect of prior-austenite grain refinement on microstructure, mechanical properties and thermal embrittlement of 9Cr-1Mo-0.2C steel, J. Nucl. Mater. 494 (2017) 260–277, https://doi.org/10.1016/j.jnucmat.2017.07.019.